folding intermediate, even when mature? Rather than being a vestige of kinase evolution with Hsp90 buffering gain-of-function destabilizing mutations (*31*), we argue that being able to safely populate such an open folding intermediate has a direct functional and regulatory benefit. Recent computational efforts have suggested a connection between folding and kinase activity (*32, 33*). The concept is that the most favorable transition between the inactive and active states is through a more open, unfolded state rather than through a more classical rigid-body transition. Although the opening seen in simulations is far more subtle than what we observed, we suggest that the concept still applies (Fig. 6A). The generally lower stability of client kinases would lead to enhanced sampling of the open state, thereby encouraging chaperone binding (Fig. 6B). Chaperone stabilization of a kinase open state could increase the overall rates of interconversion and/or protect a potentially vulnerable state from aggregation or recognition by the ubiquitinylation machinery. Moreover, the open state could be the preferred substrate for adding and removing posttranslational modifications, as well as for critical stabilizing interactions.

Life cycle of kinase-Hsp90-Cdc37 interactions

Our structure also suggests how the observed state might arise and mature (Fig. 6C). Hsp90 would first interact with Cdc37-kinase via previously published crystal structure contacts (Fig. 6C, state III). Whether assistance from Hsp70 and/or Hsp40, as with the glucocorticoid receptor, would be required is still unclear (*34*), but the inability to directly form the complex from components and Chk1 reconstitution experiments (*35*) is suggestive. During the cycle, Cdc37 would act as a quality-control checkpoint, where it would dissociate from the kinase only upon proper folding of the N lobe. The long coiled-coil would allow Cdc37-kinase to stay attached to Hsp90 during multiple ATP hydrolysis events. If the kinase would fail to dissociate after many hydrolysis events, the degradation machinery might then be recruited to the complex. Although Fig. 6C captures the essence of the available data, other models are possible.

Beyond revealing the kinase open state, our cryo-EM reconstruction allowed us to build the first atomic models for human cytosolic Hsp90 and the kinase-interacting N terminus of Cdc37. The ability to collect a large number of particles, coupled with the capabilities of single-electron–counting detectors and 3D classification software, allowed us to visualize multiple conformations, providing a qualitative assessment for the dynamic nature of the complex. Overall, our structure has enabled us to explain a number of often-contradictory biochemical observations and to provide both mechanistic and conceptual models of Hsp90-kinase interactions that can be tested in future experiments. Our structure also indicates the potential for single-particle cryo-EM to facilitate exploration of other dynamic, asymmetric complexes at near-atomic resolution.

REFERENCES AND NOTES

1. S. S. Taylor, M. M. Keshwani, J. M. Steichen, A. P. Kornev, *Philos. Trans. R. Soc. Lond. B Biol. Sci.* **367**, 2517–2528 (2012).
2. J. Zhang, P. L. Yang, N. S. Gray, *Nat. Rev. Cancer* **9**, 28–39 (2009).
3. J. A. Endicott, M. E. Noble, L. N. Johnson, *Annu. Rev. Biochem.* **81**, 587–613 (2012).
4. J. Brugge, W. Yonemoto, D. Darrow, *Mol. Cell. Biol.* **3**, 9–19 (1983).
5. M. Taipale, D. F. Jarosz, S. Lindquist, *Nat. Rev. Mol. Cell Biol.* **11**, 515–528 (2010).
6. M. Taipale *et al.*, *Cell* **150**, 987–1001 (2012).
7. Y. Miyata, H. Nakamoto, L. Neckers, *Curr. Pharm. Des.* **19**, 347–365 (2013).
8. K. A. Krukenberg, T. O. Street, L. A. Lavery, D. A. Agard, *Q. Rev. Biophys.* **44**, 229–255 (2011).
9. M. P. Mayer, L. Le Breton, *Mol. Cell* **58**, 8–20 (2015).
10. D. R. Southworth, D. A. Agard, *Mol. Cell* **32**, 631–640 (2008).
11. S. Tsutsumi *et al.*, *Proc. Natl. Acad. Sci. U.S.A.* **109**, 2937–2942 (2012).
12. J. Shao, A. Irwin, S. D. Hartson, R. L. Matts, *Biochemistry* **42**, 12577–12588 (2003).
13. S. M. Roe *et al.*, *Cell* **116**, 87–98 (2004).
14. J. M. Eckl *et al.*, *J. Biol. Chem.* **288**, 16032–16042 (2013).
15. S. Polier *et al.*, *Nat. Chem. Biol.* **9**, 307–312 (2013).
16. C. K. Vaughan *et al.*, *Mol. Cell* **31**, 886–895 (2008).
17. M. Taipale *et al.*, *Nat. Biotechnol.* **31**, 630–637 (2013).
18. E. E. Boczek *et al.*, *Proc. Natl. Acad. Sci. U.S.A.* **112**, E3189–E3198 (2015).
19. C. K. Vaughan *et al.*, *Mol. Cell* **23**, 697–707 (2006).
20. Y. Cheng, *Cell* **161**, 450–457 (2015).
21. S. D. Hartson, V. Thulasiraman, W. Huang, L. Whitesell, R. L. Matts, *Biochemistry* **38**, 3837–3849 (1999).
22. Materials and methods are available as supplementary materials on *Science* Online.
23. M. M. Ali *et al.*, *Nature* **440**, 1013–1017 (2006).
24. T. Takaki *et al.*, *Proc. Natl. Acad. Sci. U.S.A.* **106**, 4171–4176 (2009).
25. O. Genest *et al.*, *Mol. Cell* **49**, 464–473 (2013).
26. L. A. Lavery *et al.*, *Mol. Cell* **53**, 330–343 (2014).
27. J. M. Eckl *et al.*, *J. Biol. Chem.* **290**, 30843–30854 (2015).
28. W. Liu, R. Landgraf, *Biochemistry* **54**, 1493–1504 (2015).
29. P. J. Day *et al.*, *Proc. Natl. Acad. Sci. U.S.A.* **106**, 4166–4170 (2009).
30. W. Xu *et al.*, *Nat. Struct. Mol. Biol.* **12**, 120–126 (2005).
31. J. Lachowiec, T. Lemus, E. Borenstein, C. Queitsch, *Mol. Biol. Evol.* **32**, 91–99 (2015).
32. O. Miyashita, J. N. Onuchic, P. G. Wolynes, *Proc. Natl. Acad. Sci. U.S.A.* **100**, 12570–12575 (2003).
33. Y. Shan, A. Arkhipov, E. T. Kim, A. C. Pan, D. E. Shaw, *Proc. Natl. Acad. Sci. U.S.A.* **110**, 7270–7275 (2013).
34. E. Kirschke, D. Goswami, D. Southworth, P. R. Griffin, D. A. Agard, *Cell* **157**, 1685–1697 (2014).
35. S. J. Arlander *et al.*, *J. Biol. Chem.* **281**, 2989–2998 (2006).
36. Single-letter abbreviations for the amino acid residues are as follows: A, Ala; C, Cys; D, Asp; E, Glu; F, Phe; G, Gly; H, His; I, Ile; K, Lys; L, Leu; M, Met; N, Asn; P, Pro; Q, Gln; R, Arg; S, Ser; T, Thr; V, Val; W, Trp; and Y, Tyr.

QUANTUM SIMULATION

Exploring the many-body localization transition in two dimensions

Jae-yoon Choi,[1]*† Sebastian Hild,[1]* Johannes Zeiher,[1] Peter Schauß,[1]‡ Antonio Rubio-Abadal,[1] Tarik Yefsah,[1]§ Vedika Khemani,[2] David A. Huse,[2,3] Immanuel Bloch,[1,4] Christian Gross[1]

A fundamental assumption in statistical physics is that generic closed quantum many-body systems thermalize under their own dynamics. Recently, the emergence of many-body localized systems has questioned this concept and challenged our understanding of the connection between statistical physics and quantum mechanics. Here we report on the observation of a many-body localization transition between thermal and localized phases for bosons in a two-dimensional disordered optical lattice. With our single-site–resolved measurements, we track the relaxation dynamics of an initially prepared out-of-equilibrium density pattern and find strong evidence for a diverging length scale when approaching the localization transition. Our experiments represent a demonstration and in-depth characterization of many-body localization in a regime not accessible with state-of-the-art simulations on classical computers.

I n his seminal work on localization in quantum mechanical systems, Philip Anderson emphasized the implications of localization on the thermodynamics of closed quantum systems (*1*). Recently, perturbative arguments suggested the existence of nonthermalizing, many-body localized systems at low energy (*2, 3*). Soon thereafter, these arguments were extended to all interaction strengths and energy densities for systems with a bounded spectrum (*4, 5*). The implication—nothing less than a breakdown of equilibrium statistical mechanics for certain generic

macroscopic systems—triggered tremendous theoretical efforts (6–8). Furthermore, the breakdown of the eigenstate thermalization hypothesis (9–12) caused by the failure of these systems to act as their own heat bath implies the persistence of initial state information, which might serve as a useful resource for quantum information technologies (13). Several other notable features of many-body localization (MBL) have been uncovered, such as the description of fully localized systems by coupled localized integrals of motion (14, 15). This underlies the absence of particle transport but allows the transport of phase cor-

relations, leading to a characteristic logarithmic growth of the entanglement entropy in the case of short-range interactions (16–20). Another distinctive feature of many-body localized systems, as compared with noninteracting low-dimensional systems, is the requirement of a nonzero disorder strength for the localized phase to appear (21, 22).

Recently, the absence of thermalization due to MBL in a quasi-disordered one-dimensional (1D) Fermi lattice has been reported (23, 24). These studies explored the system's behavior at long times and high energy density, as opposed to earlier experiments with noninteracting systems (25–30) or interacting ultracold atoms in lower-energy states (31–36). A recent experiment with 3D disordered lattice fermions provided evidence for the absence of particle transport, even at elevated temperatures (37). Indications for localization in Fock space, one characteristic property of MBL (2), have been reported in short ion chains (38), and MBL has been suggested as one possible explanation for the recently observed vanishing conductance in disordered supercon-

ductors at nonzero temperature (39). However, despite intensive theoretical and experimental efforts, some aspects of MBL, such as the details of the localization transition, including the identification of diverging length scales, are still not fully understood. Whereas in one dimension the localization transition is rather well studied (21, 22, 40, 41), the nature of MBL in higher dimensions is an open question.

Here we address the open question of the nature of a MBL transition in two dimensions, which we observe experimentally and characterize. We report on the single-site–resolved study of thermalization and transport in a disordered 2D bosonic optical lattice, starting from a high–energy density initial state far from equilibrium. By tracking the time evolution of an initially prepared density domain wall for variable disorder strengths, we reveal the fairly sharp onset of nonthermalizing behavior above a critical value of disorder strength. The observed localization transition is found when the disorder, single-particle bandwidth, onsite interaction, and
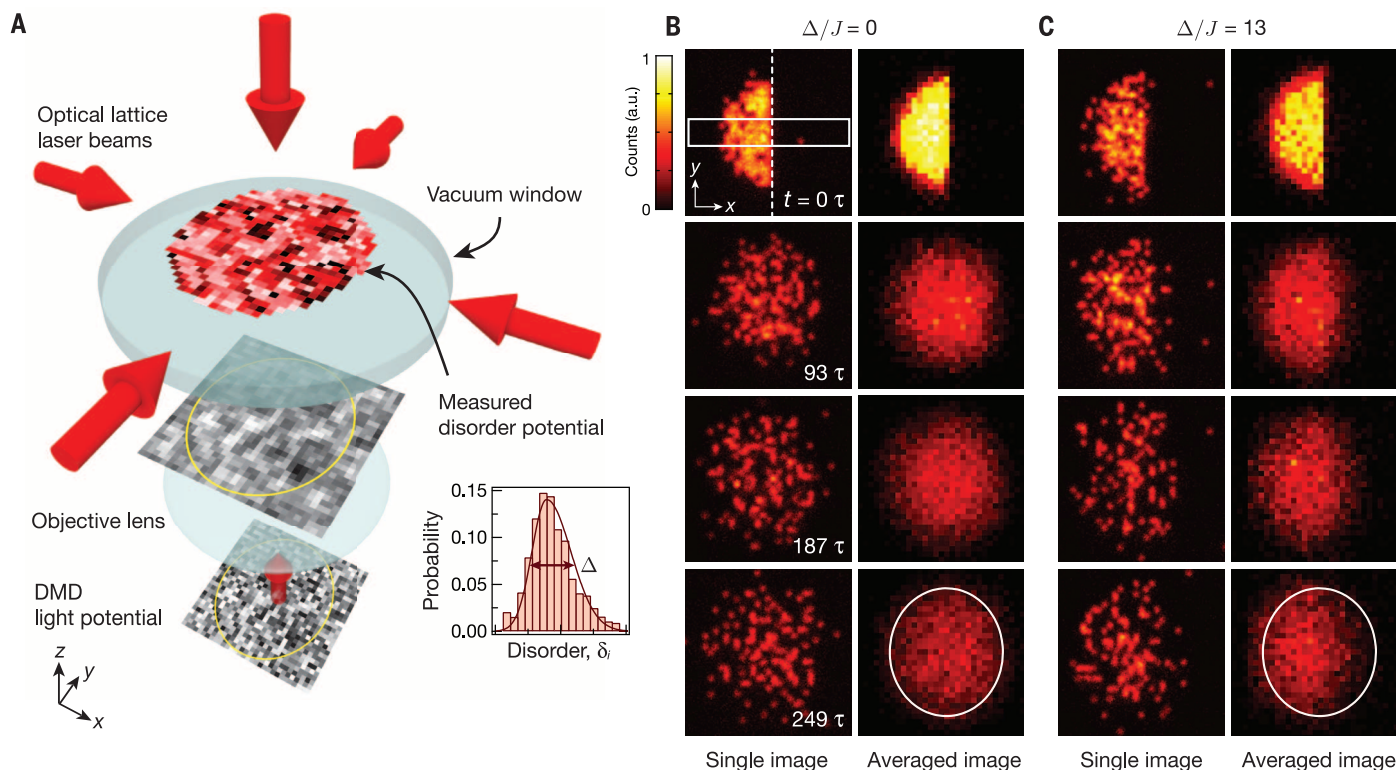
[1]Max-Planck-Institut für Quantenoptik, 85748 Garching, Germany. [2]Department of Physics, Princeton University, Princeton, NJ 08544, USA. [3]Institute for Advanced Study, Princeton, NJ 08540, USA. [4]Fakultät für Physik, Ludwig-Maximilians-Universität, 80799 München, Germany. *These authors contributed equally to this work. †Corresponding author. Email: jae-yoon.choi@mpq.mpg.de ‡Present address: Department of Physics, Princeton University, Princeton, NJ 08540, USA. §‡Present address: Laboratoire Kastler Brossel, CNRS, École Normale Supérieure, 75005 Paris, France.

Fig. 1. Schematics of the experiment and raw images. (**A**) A 2D random disorder potential is imaged onto a single atomic plane in an optical lattice. The disorder is controlled by a digital mirror device (DMD), which converts a Gaussian laser intensity profile into a 2D random intensity distribution with spatially uniform mean light intensity (bottom image). The limited numerical aperture (NA = 0.68) of the microscope objective introduces a finite correlation length and leads to a smoothing of the disorder distribution. The histogram at bottom right (red bars) is the measured disorder distribution and its asymmetric Gaussian fit curve (red solid line), where Δ is the full width at half maximum of the disorder distribution. Distinct to the other two images showing the original (bottom) and smoothed (middle) light intensity distributions, the top image displays the local disorder potential determined by in situ spectroscopy (42). The yellow circles on the lower images indicate the spectroscopically calibrated region. (**B**) Raw fluorescence images (the red-to-yellow color scale corresponds to increasing detected light level) showing the evolution of the initial density step without disorder. The left column shows single images (isolated red dots are individual atoms) of the parity-projected atomic distribution for the indicated evolution times. The right column displays the mean density distribution averaged over 50 different disorder potentials. The top left image depicts the initial state for which the analysis region ($dx \times dy = 5 \times 31$) is indicated by the white box. For the high-disorder case shown in (**C**) the detected initial-state filling is slightly lower, which is an artifact of the parity projection (42). In contrast to (B), traces of the initial state remain at all times in the disordered case. The white circles in the averaged density profiles after $t = 249\tau$ highlight the difference. a.u., arbitrary units.

energy density are all of comparable strength. This regime of parameters, being far from the disorder-dominated (classical) and the interaction-dominated limits, is highly nontrivial from a theoretical perspective. Precise and direct characterization of the projected disorder potential by site-resolved spectroscopy allows for a direct comparison of our results with a numerical prediction for the noninteracting model, highlighting the dramatic differences and pointing out the key role of interactions. Furthermore, by locally comparing the observed density profiles to a thermalizing reference measured without disorder, we obtain strong evidence for a diverging length scale when approaching the transition from the localized side.

Experimental setup

We began by preparing a 2D approximately unity filled Mott insulator of bosonic ^{87}Rb atoms in a single plane of a cubic optical lattice with lattice spacing $a_{lat} = 532$ nm. To ensure that the initial state was separable, we froze out any motion at a lattice depth of $40E_r$ in the x and y directions, where $E_r = h^2/8ma_{lat}^2$ is the recoil energy, h the Planck constant, and m is the atomic mass. Next, we used a digital mirror device–based spatial light modulator (42) to optically remove the right half of the atomic population such that about $N = 125(11)$ atoms remained in the lattice sites located at $x < 0$, thus preparing a sharp density domain wall. For each experimental realization, a new computer-generated random disorder pattern drawn from a uniform distribution was displayed on the light modulator and subsequently projected onto the atoms (Fig. 1A). The optical projection results in a slightly asymmetric disorder distribution and a convolution of the disorder, with the point spread function of the imaging system leading to a finite disorder correlation length $0.6a_{lat}$ and a narrowing of the disorder distribution to a width Δ (Fig. 1A, inset) (43). We used single-site–resolved spectroscopy of the atomic sample to directly characterize the disorder. The topmost disorder picture in Fig. 1A displays the

result of one such spectroscopic measurement for the configuration shown in the two images below. We then initiated the dynamics of the initial domain wall by lowering the x and y lattice depths to $12E_r$ in 5 ms, which is less than one tunneling time. Next, we allowed the system to evolve for a variable time t in the disorder potential, after which we used fluorescence imaging to measure the local parity-projected density (44).

During the dynamics, the system is described by a 2D Bose-Hubbard Hamiltonian with onsite disorder

$$\hat{H} = -J\sum_{\langle i,j \rangle} \hat{a}_i^\dagger \hat{a}_j + \frac{U}{2}\sum_i \hat{n}_i(\hat{n}_i - 1) + \sum_i (\delta_i + V_i)\hat{n}_i$$

Here, $\hat{a}_i^\dagger$ ($\hat{a}_i$) is the bosonic creation (annihilation) operator, $\hat{n}_i = \hat{a}_i^\dagger\hat{a}_i$ is the local density operator on site $i = (i_x, i_y)$, and the first sum includes all neighboring sites. A harmonic trapping potential $V_i = ma_{lat}^2(\omega_x^2 i_x^2 + \omega_y^2 i_y^2)/2$ with frequencies $(\omega_x, \omega_y) = 2\pi \times (54, 60)$Hz in the x and y direction confines the atoms around the trap minimum. The nearest-neighbor hopping strength at a lattice depth of $12E_r$ is $J/h = 24.8$ Hz, corresponding to a tunneling time of $\tau = h/2\pi J = 6.4$ ms. Longer-range hopping terms are neglected, as they are exponentially suppressed. The onsite interaction strength is $U = 24.4J$, and δ_i denotes the onsite disorder potential. For these parameters, in the absence of disorder, the system's ground state is in the Mott insulating phase, albeit with strong particle-hole fluctuations (45).

MBL in two dimensions

For reference, we first tracked the time evolution without any disorder potential applied. Even

Fig. 2. Relaxation dynamics of a density domain wall. The evolution of the imbalance $\mathcal{I}$ shown for five different disorder strengths [$\Delta/J = 0$ (dark green), 3 (medium green), 4 (light green), 8 (light blue), and 13 (dark blue)] displays a saturation behavior toward a quasi–steady state for all disorder strengths. For low disorders (green curves), the asymptotic value of the imbalance is vanishing, whereas a finite imbalance remains for higher disorder (blue). Solid curves are fits to the data with $\mathcal{I} = \mathcal{I}_0\exp(-t/t_s) + \mathcal{I}_\infty$, of which the decay time t_s is plotted versus disorder strength Δ in the inset. Error bars represent 1 SD of the mean in the main figure and 95% confidence bounds of the fit parameters in the inset. $\hbar$, Planck's constant h divided by 2π.
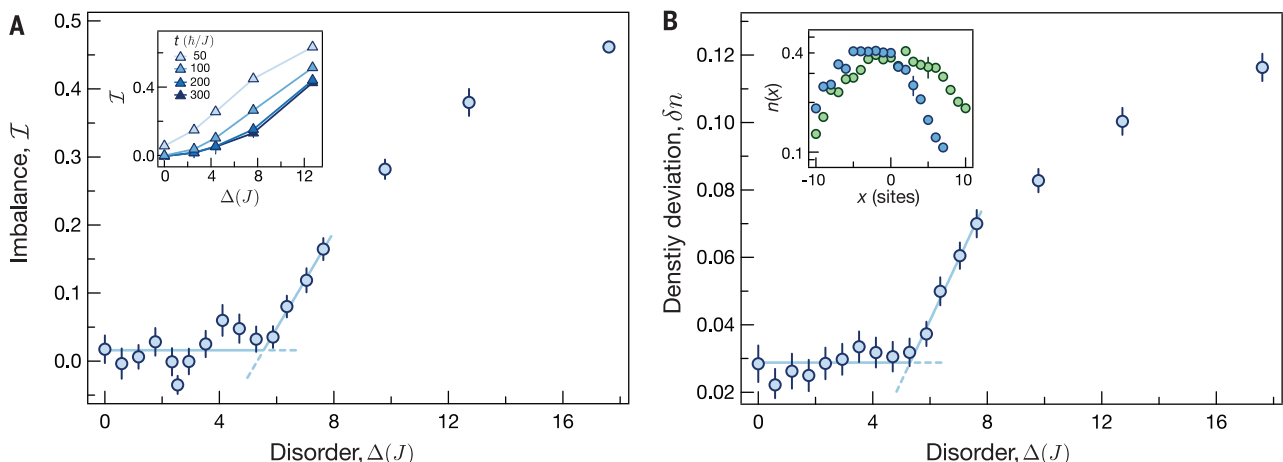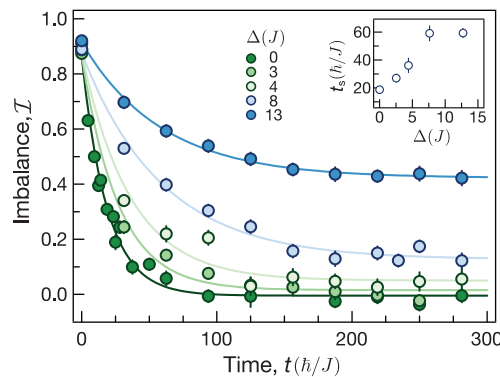

Fig. 3. Identifying the MBL transition. (**A**) Disorder dependence of the imbalance after equilibration of the dynamics [constant evolution time of 187τ also in (B)]. The data show a sharp onset of nonzero quasi–steady-state imbalance $\mathcal{I}$ at a disorder strength of $\Delta_{c,\mathcal{I}} = 5.5(4)J$, and the solid line is a double linear fit (described in the text) to extract the critical disorder. The inset illustrates the sharpening of the transition versus time and demonstrates the saturation of its shape by showing the imbalance extracted from the fits in Fig. 2

at different evolution times. (**B**) Deviation from the zero-disorder thermal profile, as measured by the root mean square density difference δn at various disorder strengths. The relaxed density profiles differ by more than the random position-induced measurement noise from the thermal profile abruptly above the critical disorder strength $\Delta_{c,\delta n} = 5.3(2)J$. The inset shows the averaged reference density profile for zero disorder (green) and the averaged profile at a high disorder of $\Delta = 13J$ (blue). Error bars represent 1 SD of the mean.
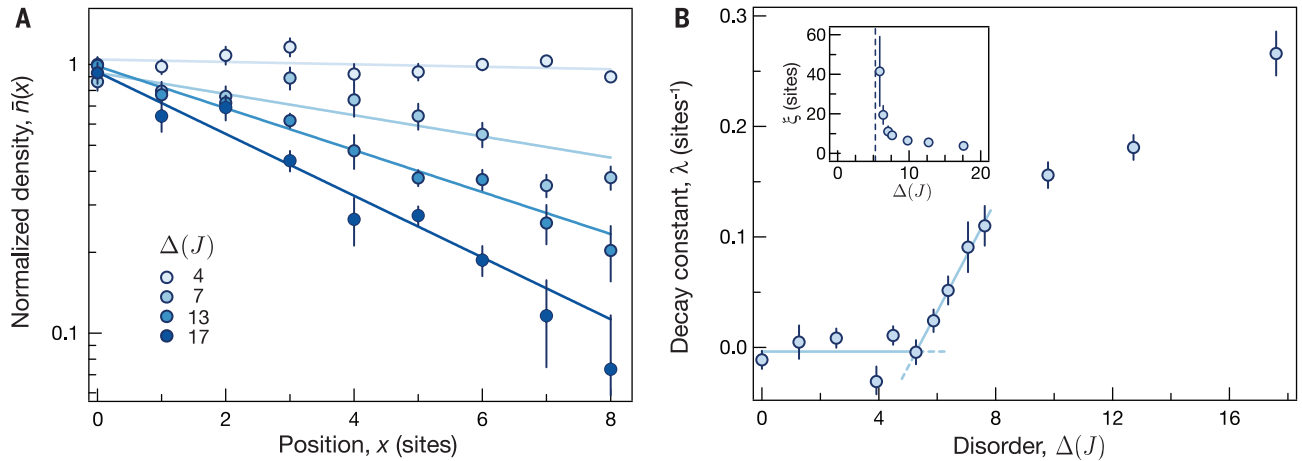
Fig. 4. Diverging density decay length at the localization transition. (**A**) The spatial dependence of the normalized average density $n(\Delta)/n(0)$ in the initially empty region is fitted by an exponentially decaying model (solid lines). The level of blue brightness encodes the disorder strength increasing from light to dark: $\Delta/J = 4, 7, 13$, and 17. (**B**) Fitted decay constant λ as a function of disorder strength Δ. The solid light blue line is a double linear fit (described in the text) to locate the transition point $\Delta_{c,\delta n} = 5.3(2)J$. The inset shows the diverging decay length $\xi = 1/\lambda$ near the critical disorder strength. Evolution time 187τ is for all data shown here. Error bars represent 1 SD of the mean in (A) and 95% confidence bounds of the fit parameters in (B).

Fig. 5. Interaction dependence of the localization transition. Quasi–steady-state imbalance $\mathcal{I}$ versus disorder strength Δ for different initial densities (evolution time 187τ). The interaction effects are reduced by lowering the initial filling to 0.23, which is 25% of the value previously discussed in Fig. 3A (light blue). The clear difference in critical disorder strengths highlights the strong influence of interactions on the localization. The right two insets show representative fluorescence images of the initial density distribution for each case. The left inset is a zoomed-out view of the main figure where we added the results of exact diagonalization numerics for the noninteracting system with the same experimental conditions (black open squares). Here, the horizontal error bars denote the systematic uncertainty in the disorder strength. Vertical error bars represent 1 SD of the mean.
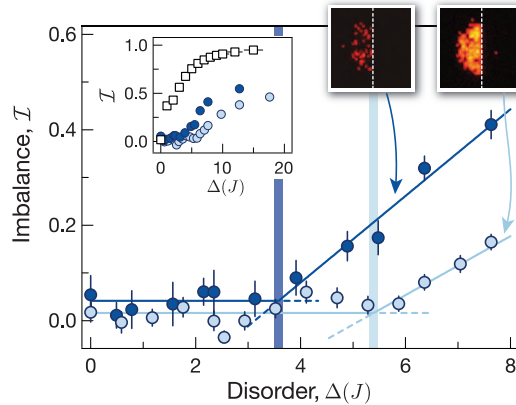
from the bare images (Fig. 1B), it is clear that the initially prepared density step is smeared out after a few tens of tunneling times τ, and after a longer time, no information about the initial density step remains. The observed density distribution appears thermal, and neglecting quantum fluctuations at $12E_r$ (that is, assuming decoupled sites), we extracted an upper limit of the temperature of $T < 0.54(1)U/k_B$, where k_B is the Boltzmann constant. This temperature estimate was obtained by a global fit to the radial density profile, assuming a grand canonical ensemble for each site with the chemical potential given by the local density approximation (*44*). The corresponding energy per particle of $E_r/N = 0.58(1)U$ might be overestimated by up to $0.15U$, due to the finite band width, and agrees reasonably well with the expectation for a thermalized state, assuming that the lattice ramp to $12E_r$ was adiabatic with respect to the band gap. Here, the energy density of the initial out-of-equilibrium state contributes

with $E_0/N = 0.28(3)U$ (where E_0 is the sum of the initial thermal and the potential energy due to the trap), determined by the initial thermal energy and the harmonic trap with frequency ω_x. An additional energy increase is present due to small heating during the 2-s evolution time [$E_H/N = 0.18(6)U$] used in this measurement (*43*). In contrast, upon repeating the measurement with strong disorder, traces of the initial state remain, and the system does not relax to a spatially symmetric density distribution expected for thermal state (Fig. 1C).

A direct and model-free quantity that can be used to identify a nonthermalized state is the density asymmetry quantified by a nonzero left (N_L) and right (N_R) atom number imbalance $\mathcal{I} = \frac{N_L - N_R}{N_L + N_R}$, which we analyze, as with all other extracted quantities, in a central region of interest extending over five lattice sites in the y direction. The zero line ($x = 0$) separating left and right is defined by the position of the initial

density step and was precisely aligned to the closest lattice site to the trap center, resulting in an offset of up to ± 1 lattice sites, corresponding to $\mathcal{I} \pm 0.05$. The evolution of the imbalance (Fig. 2) confirms that, for all disorder strengths, the system reaches a quasi–steady state within ~150τ. For small disorder strengths, we find a vanishing imbalance, whereas for large disorder, a nonzero imbalance remains, even for long evolution times. We interpret this latter regime as the many-body localized phase, where the observed quasi–steady state is clearly nonthermal and transport through the system is blocked. The relaxation time t_s, extracted from an exponential fit to the data, increases with disorder strength and hints at a saturation in the nonthermal regime (Fig. 2, inset). We now turn to a series of measurements in which we fix the evolution time to ~190τ, which is well in the quasi–steady-state regime but short enough to keep the effects of atom number loss and noise-induced coupling to higher-energy bands negligible. On this time scale, we also expect the effects of low-frequency noise on the disordered system to be small. Considering the measured heating rate in the nondisordered system as an upper bound for the energy increase, the energy per particle would change by only ~10% within one relaxation time t_s. Small couplings with the environment might lead to relaxation of the quasi–steady state on time scales much longer than our experimental time scale (*46–50*).

Identifying the MBL transition

The transition from zero to nonzero imbalance $\mathcal{I}_\infty$ for large disorder indicates the presence of a thermalizing phase for low disorder strengths and an apparent transition to a localized phase at higher disorder. To locate an MBL transition, we recorded a series of measurements with fixed evolution time in the quasi–steady-state regime and scanned the disorder around the critical value (Fig. 3). We find a fairly sharp onset of

nonzero–steady-state imbalance at a disorder strength $\Delta_{c,\mathcal{I}} = 5.5(4)J$, which indicates that the transition is taking place in the system, where we extracted the critical disorder from a simple double linear fit $\mathcal{I}(\Delta) = \mathcal{I}_0 + \mathcal{I}_1 \cdot \max[(\Delta - \Delta_{c,\mathcal{I}}), 0]$ with $\Delta/J \in [0, 8]$. In the vicinity of the transition, slow subdiffusive transport has been predicted (21, 22, 51–53), which suggests that our measurements might not have reached a true steady state in this regime. Because of this, it is possible that the resulting transition might move toward stronger disorder if we were able to study much longer times. Our high-resolution detection allows for a local comparison of the measured density profiles with the equilibrated thermal profile observed at vanishing disorder. As shown in Fig. 3B, we use this method as a more sensitive probe to detect deviations from the thermal profile by calculating the root mean square deviation $\delta n = \left\{ \sum_i [n_i(0) - n_i(\Delta)]^2 \right\}^{1/2}$ of the vertically (y direction) averaged reference profile $n_i(0) = \frac{1}{5} \sum_{j=-2}^{2} n_{i,j}(0)$ and the finite disorder profiles $n_i(\Delta)$. We observe that the profiles start to deviate at $\Delta_{c,\delta n} = 5.3(2)J$, with a fairly sharp kink signaling the transition, which is quantitatively consistent with the imbalance measurements. Whereas localization is predicted for vanishingly small disorder strength in the noninteracting case, the finite interaction U in our system promotes thermalization. This is consistent with our observation of a thermal behavior at nonzero Δ. However, as the disorder strength is increased above a critical value, the localization is restored, which is particularly notable because this transition takes place in the regime where the disorder Δ, the interaction U, and the single-particle bandwidth $8J$ are comparable.

The MBL phase transition is expected to be a continuous transition (21, 22, 40, 41, 54) for which one expects a characteristic diverging length scale when approaching the transition. With our experiments, we have direct access to the steady-state decay length $\xi(\Delta)$ of the initially prepared density step, which is directly related to a density-density correlation length. To minimize the influence of the external trap, we reference the density profile $n_i(\Delta)$ to the thermal profile $n_i(0)$ by calculating $\overline{n}_i(\Delta) = n_i(\Delta)/n_i(0)$ (Fig. 4A). The observed decay is found to be well captured by an exponential fit $\overline{n}_i(\Delta) \sim e^{-\lambda(\Delta)i}$ with a disorder-dependent decay constant $\lambda(\Delta) = 1/\xi(\Delta)$. A priori, we would have expected a crossover from an interaction-dominated decay to a single-particle–dominated decay at low densities present at the outer edge of our sample. However, within the experimental uncertainty we cannot identify such an effect. We directly observe the diverging behavior of the decay length $\xi(\Delta)$ when approaching the transition from the localized side (Fig. 4B, inset). The related decay constant $\lambda(\Delta)$ also shows a very sharp kink at $\Delta_{c,\lambda} = 5.3(3)J$, marking the onset of the localized region. We empirically obtain the critical disorder Δ_c using the bilinear fit function, $\lambda(\Delta) =$

$\lambda_0 + \lambda_1 \cdot \max[(\Delta - \Delta_{c,\lambda}), 0]$ with $\Delta/J \in [0, 8]$. We emphasize, that all three methods of extracting the critical disorder strength of the MBL transition in the experiments agree within the fit errors.

Interaction dependence

To experimentally verify that the observed behavior of the system is induced by interactions, we reduced the initial density and, therefore, the effects of the interaction on the dynamics while keeping the initial energy per particle (E_0/N) constant. Lower atomic densities are obtained by uniformly transferring a given fraction of the atoms by applying a microwave pulse to another hyperfine state and then optically removing the transferred population. When we reduced the density by factor of 4, we observed a clear shift of the localization transition toward lower disorder strength, as was expected (Fig. 5). Here, the left-right imbalance $\mathcal{I}(\Delta)$ displays a sharp transition behavior at a smaller critical disorder of $\Delta_{c,\mathcal{I}} \simeq 3.6(2)J$. Furthermore, the numerical prediction for a noninteracting system obtained by exact diagonalization (43) is fully incompatible and strongly differs from both measurements, showing that the interactions facilitate thermalization for low disorder strengths. Reducing the system size by the preparation of a smaller initial Mott insulator did not affect the observed critical disorder (43). From these observations, we conclude that the nonzero critical disorder strength is due to the interactions and that the measured critical disorder value is not strongly influenced by the small external driving caused by laser fluctuations discussed above.

Conclusions

Our experiments provide evidence for MBL in two dimensions by the observation of a transition from a thermalizing phase to a localized phase of interacting bosons in a disordered optical lattice. The system size analyzed in our experiment is far beyond numerically accessible scales, demonstrating a nontrivial quantum realization of the MBL system that challenges both analytical and numerical theory. Furthermore, we supplemented our observation of an MBL transition with the demonstration of a clear shift of the transition point for effectively smaller interaction energy. Even though it is difficult to distinguish a true phase transition from a sharp crossover within experiments, our results mark a first step in understanding MBL in more than one dimension and can be extended to obtain detailed information about the nature of the MBL transition, such as its dynamical critical exponent (21, 22). Furthermore, supplementing transport experiments with density-density correlation measurements, or even measurements of the entanglement entropy (55, 56), offers a promising possibility to demonstrate ongoing phase dynamics in the localized phase while the density or charge transport is frozen (38, 57). Via detailed studies of the dynamics of transport, it should also be possible to study Griffiths effects and subdiffusive transport in the vicinity of the

transition (21, 22, 51–53). In addition to dynamical properties, our technique might allow the investigation of many-body eigenstate–related properties, such as the local integrals of motion (14, 15) defined via local operators (54).

REFERENCES AND NOTES

1. P. W. Anderson, *Phys. Rev.* **109**, 1492–1505 (1958).
2. D. Basko, I. Aleiner, B. Altshuler, *Ann. Phys.* **321**, 1126–1205 (2006) and references therein.
3. I. V. Gornyi, A. D. Mirlin, D. G. Polyakov, *Phys. Rev. Lett.* **95**, 206603 (2005) and references therein.
4. I. L. Aleiner, B. L. Altshuler, G. V. Shlyapnikov, *Nat. Phys.* **6**, 900–904 (2010).
5. V. Oganesyan, D. A. Huse, *Phys. Rev. B* **75**, 155111 (2007).
6. R. Nandkishore, D. A. Huse, *Annu. Rev. Condens. Matter Phys.* **6**, 15–38 (2015).
7. E. Altman, R. Vosk, *Annu. Rev. Condens. Matter Phys.* **6**, 383–409 (2015).
8. J. Eisert, M. Friesdorf, C. Gogolin, *Nat. Phys.* **11**, 124–130 (2015).
9. J. M. Deutsch, *Phys. Rev. A* **43**, 2046–2049 (1991).
10. M. Srednicki, *Phys. Rev. E* **50**, 888–901 (1994).
11. H. Tasaki, *Phys. Rev. Lett.* **80**, 1373–1376 (1998).
12. M. Rigol, V. Dunjko, M. Olshanii, *Nature* **452**, 854–858 (2008).
13. M. Serbyn et al., *Phys. Rev. Lett.* **113**, 147204 (2014).
14. M. Serbyn, Z. Papić, D. A. Abanin, *Phys. Rev. Lett.* **111**, 127201 (2013).
15. D. A. Huse, R. Nandkishore, V. Oganesyan, *Phys. Rev. B* **90**, 174202 (2014).
16. M. Žnidarič, T. Prosen, P. Prelovšek, *Phys. Rev. B* **77**, 064426 (2008).
17. J. H. Bardarson, F. Pollmann, J. E. Moore, *Phys. Rev. Lett.* **109**, 017202 (2012).
18. R. Vosk, E. Altman, *Phys. Rev. Lett.* **110**, 067204 (2013).
19. M. Serbyn, Z. Papić, D. A. Abanin, *Phys. Rev. Lett.* **110**, 260601 (2013).
20. A. Nanduri, H. Kim, D. A. Huse, *Phys. Rev. B* **90**, 064201 (2014).
21. A. C. Potter, R. Vasseur, S. Parameswaran, *Phys. Rev. X* **5**, 031033 (2015).
22. R. Vosk, D. A. Huse, E. Altman, *Phys. Rev. X* **5**, 031032 (2015).
23. M. Schreiber et al., *Science* **349**, 842–845 (2015).
24. P. Bordia et al., *Phys. Rev. Lett.* **116**, 140401 (2016).
25. T. Schwartz, G. Bartal, S. Fishman, M. Segev, *Nature* **446**, 52–55 (2007).
26. J. Billy et al., *Nature* **453**, 891–894 (2008).
27. G. Roati et al., *Nature* **453**, 895–898 (2008).
28. S. S. Kondov, W. R. McGehee, J. J. Zirbel, B. DeMarco, *Science* **334**, 66–68 (2011).
29. F. Jendrzejewski et al., *Nat. Phys.* **8**, 398–403 (2012).
30. G. Semeghini et al., *Nat. Phys.* **11**, 554–559 (2015).
31. B. Deissler et al., *Nat. Phys.* **6**, 354–358 (2010).
32. M. Pasienski, D. McKay, M. White, B. DeMarco, *Nat. Phys.* **6**, 677–680 (2010).
33. B. Gadway, D. Pertot, J. Reeves, M. Vogt, D. Schneble, *Phys. Rev. Lett.* **107**, 145306 (2011).
34. C. D'Errico et al., *Phys. Rev. Lett.* **113**, 095301 (2014).
35. L. Tanzi et al., *Phys. Rev. Lett.* **111**, 115301 (2013).
36. C. Meldgin et al., *Nat. Phys.* 10.1038/nphys3695 (2016).
37. S. S. Kondov, W. R. McGehee, W. Xu, B. DeMarco, *Phys. Rev. Lett.* **114**, 083002 (2015).
38. J. Smith et al., *Nat. Phys.* 10.1038/nphys3783 (2016).
39. M. Ovadia et al., *Sci. Rep.* **5**, 13503 (2015).
40. A. Pal, D. A. Huse, *Phys. Rev. B* **82**, 174411 (2010).
41. J. A. Kjäll, J. H. Bardarson, F. Pollmann, *Phys. Rev. Lett.* **113**, 107204 (2014).
42. C. Weitenberg et al., *Nature* **471**, 319–324 (2011).
43. See supplementary materials on *Science* Online.
44. J. F. Sherson et al., *Nature* **467**, 68–72 (2010).
45. M. Endres et al., *Science* **334**, 200–203 (2011).
46. R. Nandkishore, S. Gopalakrishnan, D. A. Huse, *Phys. Rev. B* **90**, 064203 (2014).
47. S. Johri, R. Nandkishore, R. N. Bhatt, *Phys. Rev. Lett.* **114**, 117401 (2015).
48. E. Levi, M. Heyl, I. Lesanovsky, J. P. Garrahan, *Phys. Rev. Lett.* **116**, 237203 (2016).

49. M. V. Medvedyeva, T. Prosen, M. Žnidarič, *Phys. Rev. B* **93**, 094205 (2016).
50. M. H. Fischer, M. Maksymenko, E. Altman, *Phys. Rev. Lett.* **116**, 160401 (2016).
51. Y. Bar Lev, G. Cohen, D. R. Reichman, *Phys. Rev. Lett.* **114**, 100601 (2015).
52. K. Agarwal, S. Gopalakrishnan, M. Knap, M. Müller, E. Demler, *Phys. Rev. Lett.* **114**, 160401 (2015).
53. Y. B. Lev, D. R. Reichman, *Europhys. Lett.* **113**, 46001 (2016).
54. A. Chandran, I. H. Kim, G. Vidal, D. A. Abanin, *Phys. Rev. B* **91**, 085425 (2015).
55. R. Islam *et al*., *Nature* **528**, 77–83 (2015).
56. A. M. Kaufmann *et al*., http://arxiv.org/abs/1603.04409 (2016).
57. M. Goihl, M. Friesdorf, A. H. Werner, W. Brown, J. Eisert, http://arxiv.org/abs/1601.02666 (2016).

REPORTS

QUANTUM PHYSICS

Quantum phase magnification

O. Hosten, R. Krishnakumar, N. J. Engelsen, M. A. Kasevich*

Quantum metrology exploits entangled states of particles to improve sensing precision beyond the limit achievable with uncorrelated particles. All previous methods required detection noise levels below this standard quantum limit to realize the benefits of the intrinsic sensitivity provided by these states. We experimentally demonstrate a widely applicable method for entanglement-enhanced measurements without low-noise detection. The method involves an intermediate quantum phase magnification step that eases implementation complexity. We used it to perform squeezed-state metrology 8 decibels below the standard quantum limit with a detection system that has a noise floor 10 decibels above the standard quantum limit.

The prospect of using quantum entanglement to improve the precision of atomic and optical sensors has been a topic of discussion for more than two decades. Examples of recent work using atomic ensembles include the preparation of spin-squeezed states (*1–12*), Dicke states (*13–15*), and other states with negative Wigner functions (*16*). An assumption common to all this work is that low-noise detection methods are required to properly measure and make use of the prepared quantum states. In fact, detection noise has thus far been the bottleneck in the performance of these systems. To this end, there has been dedicated work on improving state-selective detection of atoms with both optical cavity–aided measurements (*17, 18*) and fluorescence imaging (*19, 20*).

Here, we describe the concept and the implementation of a quantum phase magnification technique that relaxes stringent requirements in detection sensitivity for quantum metrology. This method is a generalization of a recent proposal for approaching the Heisenberg limit in measurement sensitivity without single-particle detection (*21*). We demonstrate the method in an ensemble of ^{87}Rb atoms. As in a typical atomic sensor or clock, the goal is to measure a differential phase shift accumulated between a pair of quantum states during a time interval. Making this measurement requires the phase shift to be converted into

Department of Physics, Stanford University, Stanford, CA 94305, USA.
*Corresponding author. Email: kasevich@stanford.edu

a population difference (*12, 22*), after which the population difference is measured. Our scheme magnifies this population difference before the final detection, in effect magnifying the initial phase shift. The atomic ensemble is first spin-squeezed using atomic interactions aided by an optical cavity, and then small rotations—to be sensed—are induced on the atomic state. These rotations are magnified by stretching the rotated states (Fig. 1A), using cavity-aided interactions, and are finally detected via fluorescence imaging. Magnification allows for substantial reduction in the noise requirements for the final detection. Although the method is demonstrated in an atom/cavity system, it is broadly applicable to any quantum system that has a suitable nonlinear interaction [see below and (*23*)].

The collective state of an ensemble of N two-level atoms—here, the clock states of ^{87}Rb—can be described using the language of a pseudo–spin-$N/2$ system. The z-component of the spin, J_z, represents the population difference, and the orientation in the J_x - J_y plane represents the phase difference between the two states. As these angular momentum components do not commute, both the population and the phase possess uncertainties. For a state with $\langle J_x \rangle \approx N/2$, the uncertainties satisfy $\Delta J_z \cdot \Delta J_y \geq N/4$, where J_y is now identified with the phase of the ensemble. Coherent spin states (CSS) with noise $\Delta J_z = \Delta J_y = \sqrt{N}/2 \equiv \Delta_{CSS}$ establish the standard quantum limit (SQL) to minimum resolvable phase or population difference.

The magnification procedure (Fig. 1A) starts with a mapping of J_z onto J_y (Fig. 1B) via a shearing interaction. A rotation of J_y into J_z follows to complete the sequence. The interaction leading to the mapping (shearing) generates a rotation of the state about the J_z axis, with the rotation rate depending on J_z, and is represented by the one-axis twisting Hamiltonian (*24*) $H = \hbar \chi J_z^2$, where $\hbar$ is the Planck constant divided by 2π and χ is the shearing strength.

The Heisenberg equations of motion for the vector operator **J** yield $dJ/dt = \frac{1}{2}(\Omega \times \mathbf{J} - \mathbf{J} \times \Omega)$, where the rotation vector $\Omega = \hat{z}2\chi J_z$ is also an operator, and $\hat{z}$ is a unit vector in the z-direction. We assume that the angular shifts we seek to measure are small (otherwise, they would readily be measurable without magnification) and that the uncertainties of the states after magnification occupy a small fraction of the Bloch sphere. With these assumptions and working with near-maximal initial x-polarization $J_x \approx J = N/2$, we can linearize the problem and focus our attention to a planar patch of the spherical phase space (Fig. 1, B to D). The equations of motion then yield $J_z(t) = J_z(0)$ and $J_y(t) = J_y(0) + MJ_z(0)$ with $M = N\int_0^t dt' \chi(t')$. Thus, the initial J_z is mapped onto J_y with a magnification factor M. This is analogous to free expansion of a gas if one identifies J_z with a particle's momentum and J_y with its position.

We implement the one-axis twisting Hamiltonian through a dispersive interaction between atoms and light in an optical cavity (*1*) (Fig. 2A). The underlying mechanism is a coupling between the intracavity power and atomic populations. The atom-cavity detuning is set such that the shift in the cavity resonance due to the atoms is proportional to J_z (Fig. 2C). Thus, J_z sets the cavity-light detuning, which in turn sets the intracavity power (Fig. 2D), which in turn provides a J_z-dependent ac-Stark shift—hence the J_z^2 interaction. Implemented this way, there is also a J_z-independent part of the ac-Stark shift, causing global rotations of the state about the J_z axis even for $J_z = 0$. The rotation angle ϕ_{AC} due to this effect is proportional to the pulse area of the interaction light incident on the cavity. By directly measuring ϕ_{AC} and offsetting the phase of the microwave oscillator by the same amount, we effectively work in a frame where the center of the states remains in the J_x - J_z plane (*23*). The magnification parameter

$$M = N\frac{\delta_c \delta_0}{\delta_0^2 + (\kappa/2)^2} \phi_{AC} \qquad (1)$$

obtained in this implementation directly relates to the measured quantity ϕ_{AC}. Here, $\delta_c = 5.5$ Hz is the

Science

Exploring the many-body localization transition in two dimensions

Jae-yoon Choi, Sebastian Hild, Johannes Zeiher, Peter Schauß, Antonio Rubio-Abadal, Tarik Yefsah, Vedika Khemani, David A. Huse, Immanuel Bloch and Christian Gross

Bosons refusing to thermalize in 2D

Messy, interacting quantum-mechanical systems are difficult to analyze theoretically. In a single spatial dimension, the calculations are still tractable, and experiments have recently confirmed the prediction that sufficiently strong disorder can disrupt the transport of interacting particles. In two dimensions, however, the theoretical blueprint is missing. Choi *et al.* used single-site imaging of cold ^{87}Rb atoms in an optical lattice to show that similar localization occurs in two-dimensional (2D) systems. The study highlights the power of quantum simulation to solve problems that are currently inaccessible to classical computing techniques.

Science, this issue p. 1547